PHYSICAL REVIEW C **86**, 011305(R) (2012)

Intermediate-energy Coulomb excitation of ^{58,60,62}Cr: The onset of collectivity toward $N = 40$

T. Baugher,[1,2,*] A. Gade,[1,2] R. V. F. Janssens,[3] S. M. Lenzi,[4] D. Bazin,[1] B. A. Brown,[1,2] M. P. Carpenter,[3] A. N. Deacon,[5] S. J. Freeman,[5] T. Glasmacher,[1,2] G. F. Grinyer,[1,†] F. G. Kondev,[3] S. McDaniel,[1,2] A. Poves,[6] A. Ratkiewicz,[1,2] E. A. McCutchan,[3] D. K. Sharp,[5] I. Stefanescu,[3] K. A. Walsh,[1,2] D. Weisshaar,[1] and S. Zhu[3]

[1]*National Superconducting Cyclotron Laboratory, Michigan State University, East Lansing, Michigan 48824, USA*

[2]*Department of Physics and Astronomy, Michigan State University, East Lansing, Michigan 48824, USA*

[3]*Physics Division, Argonne National Laboratory, Argonne, Illinois 60439, USA*

[4]*Dipartimento di Fisica e Astronomia dell'Università and INFN, Sezione di Padova, I-35131 Padova, Italy*

[5]*School of Physics and Astronomy, Schuster Laboratory, University of Manchester, Manchester M13 9PL, United Kingdom*

[6]*Departamento de Física Teórica e IFT-UAM/CSIC, Universidad Autónoma de Madrid, E-28049 Madrid, Spain*

(Received 16 May 2012; published 26 July 2012)

Intermediate-energy Coulomb excitation measurements were performed on the neutron-rich isotopes ^{58,60,62}Cr. The electric quadrupole excitation strengths, $B(E2; 0_1^+ \rightarrow 2_1^+)$, of ^{60,62}Cr are determined for the first time. The results quantify the trend of increasing quadrupole collectivity in the Cr isotopes approaching neutron number $N = 40$. The results are confronted with large-scale shell-model calculations in the $fpgd$ shell using the state-of-the-art LNPS effective interaction. Different sets of effective charges are discussed that provide an improved and robust description of the $B(E2)$ values of the neutron-rich Fe and Cr isotopes in this region of rapid shell evolution. The ratio of the neutron and proton transition matrix elements, $|M_n/M_p|$, is proposed as an effective tool to discriminate between the various choices of effective charges.

DOI: 10.1103/PhysRevC.86.011305 PACS number(s): 23.20.−g, 21.60.Cs, 25.70.De, 27.50.+e

Nuclear shell structure is well established for stable nuclei. Beyond the valley of β stability, some of the canonical magic numbers disappear and new ones emerge [1,2]. Spin-isospin parts of the NN interaction, in particular the monopole components of the proton-neutron tensor force, have been identified as robust driving forces for shell evolution in exotic systems [3–5]. The chain of nuclei with neutron number $N = 40$, a harmonic-oscillator magic number and subshell gap, is particularly interesting. Along this isotonic line, the $N = Z = 40$ nucleus ^{80}Zr is highly deformed with a quadrupole deformation parameter of $\beta_2 \approx 0.4$ [6]. On the neutron-rich end of this line, ^{68}Ni has its first 2^+ state near 2 MeV and a small $B(E2; 0_1^+ \rightarrow 2_1^+)$ transition probability [7], with a highly deformed proton intruder 0^+ state predicted at about 2.2 MeV [8] and a candidate state identified in Ref. [9].

Only two and four protons away from ^{68}Ni, the first 2^+ states of ^{66}Fe and ^{64}Cr are low lying in energy with evidence for collectivity [10,11]. A variety of complementary experimental studies have elucidated the influence of the $N = 40$ energy gap on the structure of ^{68}Ni [7,12–15], with theoretical models suggesting that below $Z = 28$ the decreased occupation of the $\pi 0f_{7/2}$ orbital leads to an onset of collectivity and deformation [7,16–18].

These structural changes are strongly influenced by the $\nu 0g_{9/2}$ and $\nu 1d_{5/2}$ neutron orbitals [16,18]. The proton-neutron tensor force between the $\pi 0f_{7/2}$ and $\nu 0f_{5/2}$ orbitals is attractive and strongest when both are fully occupied [4], as is the case for ^{68}Ni. This attraction draws the $\nu 0f_{5/2}$ orbital down in energy, creating an $N = 40$ gap of about 3 MeV [18]. Moving to Fe ($Z = 26$) and Cr ($Z = 24$) progressively weakens the monopole parts of the proton-neutron tensor interaction and shrinks the $N = 40$ gap by about 1 MeV, while the quadrupole-correlated ($\Delta\ell = 2$) $0g_{9/2}$ and $1d_{5/2}$ orbitals become nearly degenerate, enhancing the probability of their occupation by neutrons [18].

Recent excited-state lifetime measurements on neutron-rich Fe isotopes have quantified the increased collectivity in ^{64,66}Fe [19,20] through the extracted $B(E2; 0_1^+ \rightarrow 2_1^+)$ values. The chain of Cr isotopes displays a particularly rich picture of shell evolution: Stable ^{52}Cr exhibits the expected signatures of the $N = 28$ neutron shell closure, while four neutrons heavier, ^{56}Cr reveals the presence of a new shell gap at $N = 32$ [21], generated by the same robust driving force that is behind the onset of collectivity toward $N = 40$ [3]. Adding more neutrons leads to strongly increasing collectivity, with experimental evidence coming from decreasing 2_1^+ energies out to $N = 40$ [11], increasing $B(E2)$ values out to $N = 34$ [22], and increasing deformation parameters out to $N = 38$ [23] as well as the presence of rotational bands at higher spin in $^{55-59}$Cr [24–26]. The intermediate-energy Coulomb excitation measurements of ^{58,60,62}Cr reported here quantify the onset of collectivity with N in neutron-rich Cr nuclei further with extracted $B(E2; 0_1^+ \rightarrow 2_1^+)$ values. They also benchmark the latest nuclear models in this region of rapid structural change.

The measurements were performed at the Coupled Cyclotron Facility (CCF) of the National Superconducting Cyclotron Laboratory (NSCL). Secondary cocktail beams containing ^{58,60,62}Cr were produced in the projectile fragmentation of a 130-MeV/nucleon ^{76}Ge beam on a 423-mg/cm^2 ^{9}Be production target located at the entrance of the A1900 fragment separator [27]. The secondary beam cocktails were selected and purified with a 300-mg/cm^2 Al wedge in the A1900

*baugher@nscl.msu.edu

†Present address: Grand Accélérateur National d'Ions Lourds (GANIL), CEA/DSM-CNRS/IN2P3, Bvd Henri Becquerel, 14076 Caen, France.

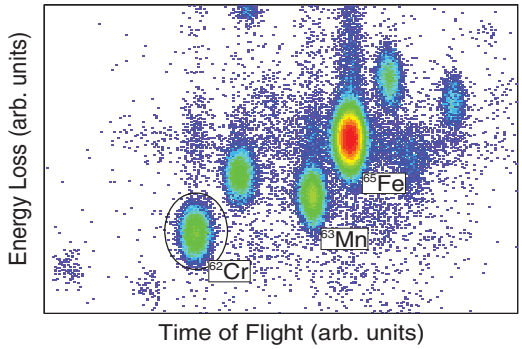

FIG. 1. (Color online) The particle identification matrix for the ^{62}Cr setting. The isotope of interest can be cleanly separated from the other components of the beam.

separator and delivered to the experimental setup. The momentum acceptance of the separator was set to 0.5% for ^{58}Cr and 3% for ^{60,62}Cr. The beams were guided onto a 252-mg/cm^2 ^{197}Au target, for ^{58,60}Cr, and a 238.4-mg/cm^2 ^{209}Bi target, for ^{62}Cr, located at the pivot point of the S800 spectrograph [28] to induce Coulomb excitation with midtarget energies of 81.1, 81.7, and 79.0 MeV/nucleon for ^{58,60,62}Cr, respectively.

The scattered projectiles exiting the target were identified on an event-by-event basis with the focal-plane detector system [29] of the S800 spectrograph. Energy loss, measured by the S800 ionization chamber, and time-of-flight information, measured between two plastic scintillators, were used to construct particle identification matrices to select the scattered projectiles of interest. The matrix for the most exotic case, ^{62}Cr, is provided in Fig. 1. The two position-sensitive cathode readout drift chambers (CRDCs) of the S800 focal plane provide xy information which, when combined with ray tracing in the spectrograph, allows for an event-by-event determination of the projectile's scattering angle at the target position.

The segmented germanium array (SeGA) [30], consisting of 17, 32-fold segmented, high-purity germanium detectors, surrounded the Coulomb excitation target in front of the S800 spectrograph to detect the de-excitation γ rays. The high degree of segmentation of the SeGA detectors enabled event-by-event Doppler reconstruction of γ rays emitted in flight by the scattered projectiles with velocities $v \approx 0.4c$. The detector segment that registered the highest energy deposition was used to determine the γ-ray emission angle for the Doppler reconstruction. Ten detectors were placed in a ring at 90° with respect to the beam axis and the remaining seven equipped the forward ring at 37°. The γ-ray detection efficiency of SeGA was determined with standard calibration sources. GEANT4 [31] simulations were used to obtain the response of the array. The simulations reproduced the measured efficiency of the setup to within 2%.

In intermediate-energy Coulomb excitation, the collision occurs above the Coulomb barrier for all projectile-target combinations, so care must be taken to ensure that nuclear contributions to the excitation are minimized. This can be accomplished by restricting the analysis to events with the most forward scattering angles, corresponding to collisions with large impact parameters. The minimum impact parameter $b_{\min}$ which corresponds to a maximum scattering angle $\theta_{\max}$

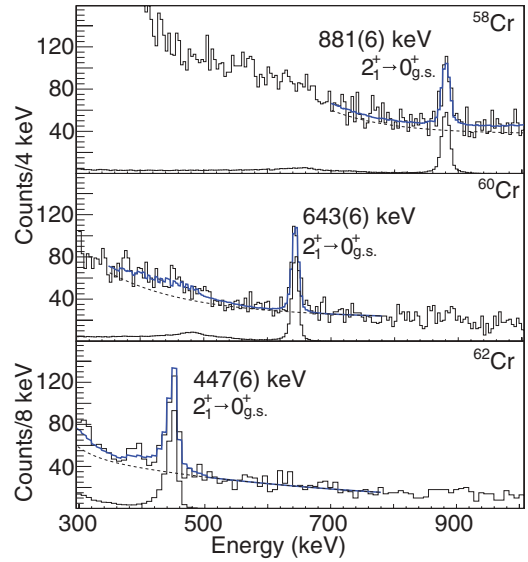

FIG. 2. (Color online) Event-by-event Doppler-corrected γ-ray spectra measured in coincidence with ^{58,60,62}Cr projectiles with scattering angles less than $\theta_{\max}$ for the respective beam-target combination. Also shown are GEANT simulations of the response of SeGA to γ rays emitted in flight from Cr nuclei as they pass through the target. Fits of the simulations to the data are in blue and the background used in the fit is given as a dashed line.

was chosen as $b_{\min} = r_0(A_{\text{target}}^{1/3} + A_{\text{projectile}}^{1/3}) + 2$ fm, where $r_0 = 1.25$ fm [1,32]. For the present cases, $b_{\min}$ corresponds to maximum laboratory scattering angles, $\theta_{\max}^{\text{lab}}$, of 2.42°, 2.33°, and 2.39° for ^{58,60,62}Cr, respectively.

Figure 2 presents the Doppler-corrected γ-ray spectra detected in coincidence with ^{58,60,62}Cr projectiles with scattering angles of $\theta \leqslant \theta_{\max}$. In each case, only the $2_1^+ \rightarrow 0_1^+$ transition was observed. Overlaid on the measured spectra are the simulated (GEANT4) responses of SeGA to γ rays emitted in flight by the Cr nuclei as they pass through the target. Fits of the simulations to the data were performed to extract the number of γ rays emitted in each case. For this purpose, a sum of two exponentials was used to model the smooth background. The simulations accounted for absorption in the target and for the angular distribution of the γ rays inherent to the Coulomb excitation process. The peak shape of the 446-keV, $2_1^+ \rightarrow 0_1^+$ transition in ^{62}Cr exhibits a pronounced left tail which is indicative of an excited-state lifetime of the order of hundreds of picoseconds. GEANT4 simulations were performed for 10 different level lifetimes between 70 and 250 ps and the resulting peak shapes were fit to the measured spectra in a χ^2 minimization. The best fit and the χ^2 as a function of the simulated lifetime can also be found in Fig. 3. From this peak-shape analysis, the lifetime of the first 2^+ state in ^{62}Cr was determined to be $\tau = 144^{+27}_{-22}$ ps, offering an independent way to extract the corresponding $B(E2)$ value.

Angle-integrated Coulomb excitation cross sections for projectile scattering angles from 0 to $\theta_{\max}$ were determined for the $0_1^+ \rightarrow 2_1^+$ excitations in ^{58,60,62}Cr from the number of γ rays relative to the number of incoming projectiles and target atoms to be $\sigma(^{58}\text{Cr}) = 185(19)$ mb, $\sigma(^{60}\text{Cr}) = 237(17)$ mb, and $\sigma(^{62}\text{Cr}) = 377(30)$ mb. These cross sections include

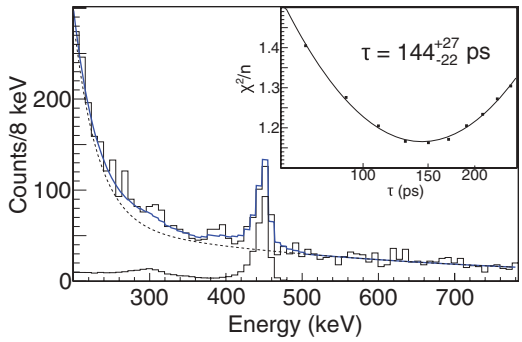

FIG. 3. (Color online) Event-by-event Doppler corrected γ-ray spectrum measured in coincidence with ^{62}Cr particles. The low-energy tail is apparent. Overlaid in blue is a fit of the simulated γ-ray response of SeGA for an excited-state lifetime of 144 ps. The background used in the fit is shown as a dashed line. The inset shows the reduced χ^2 of the fit as a function of simulated excited-state lifetime (see text for details).

uncertainties due to the fitting procedure used to determine the number of γ rays (10% for ^{58}Cr, 7% for ^{60}Cr, and 8% for ^{62}Cr), and uncertainties in the measured and simulated detection efficiency (2% each). The extracted $B(E2)$ values, shown in Table I, include additional uncertainties due to the scattering-angle reconstruction (5%) and v/c determination (5%). All uncertainties were added in quadrature. In the measurement aimed at ^{58,60}Cr, the target Coulomb excitation of the first excited $7/2^+$ state at 548 keV in ^{197}Au was observed and evaluated as a test of both the setup and the analysis procedure. For ^{62}Cr, a ^{209}Bi target was used as the 548-keV transition originating from the Coulomb excitation of a ^{197}Au target would have contaminated the ^{62}Cr γ-ray transition after Doppler reconstruction. At the present level of statistics, the Coulomb excitation cross sections to excited states in ^{209}Bi are below the sensitivity limit.

The measured cross sections were translated into $B(E2; 0_1^+ \rightarrow 2_1^+)$ values following [33]. The results are summarized in Table I. The $B(E2)$ value for ^{58}Cr is in agreement with the measurement of Ref. [22], the only instance in the current study for which a $B(E2)$ value had previously been reported. The $B(E2)$ values for ^{62}Cr determined from Coulomb excitation and from the γ-ray line-shape measurement agree well. In the

TABLE I. Measured $B(E2)$ values for projectile and target excitations and $|M_n/M_p|$ ratios relative to N/Z.

Beam	$B(E2; 0_1^+ \rightarrow 2_1^+)$ (e^2fm^4) Cr	$B(E2; 3/2_1^+ \rightarrow 7/2_1^+)$ (e^2fm^4) ^{197}Au	$\lvert M_n/M_p\rvert$ (N/Z)
^{58}Cr	860(125)	4002(610)	
	990(280) [22]	4494(410) [34]	
^{60}Cr	1105(145)	3678(910)	0.87(19)
		4494(410) [34]	
^{62}Cr	1625(220)		0.89(17)
	1605^{+302}_{-246}[a]		

[a]From the lifetime deduced from the line-shape analysis and with the adopted value of $E(2^+) = 446(1)$ keV [35] (see text).

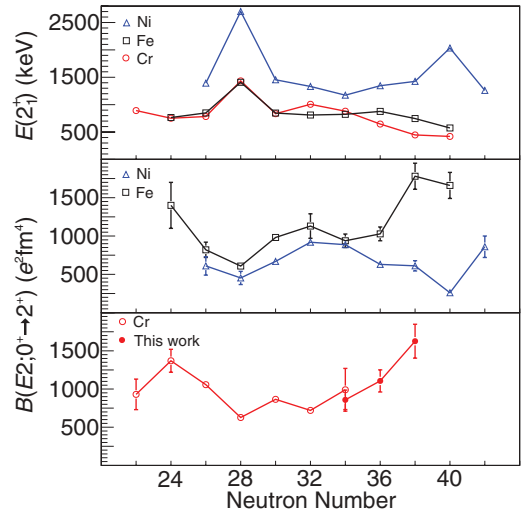

FIG. 4. (Color online) Systematics of $E(2_1^+)$ energies (top panel) and $B(E2)$ values for Ni, Fe (middle panel), and Cr (bottom panel) isotopes. Values obtained in the current work are plotted as solid circles. Other data are taken from [42,43].

two cases where the gold target was used, the $B(E2;3/2_1^+ \rightarrow 7/2_1^+)$ excitation strengths for ^{197}Au were found to be consistent with the literature value of 4494(410) e^2fm^4 [34] within the uncertainties.

Where data were available (^{60,62}Cr) [23], deformation lengths reported from (p, p') measurements were combined with the $B(E2)$ values from the current work to compute ratios of neutron-to-proton transition matrix elements, $|M_n/M_p|/(N/Z)$ following the method detailed by Riley *et al.* [36], based on the prescription by Bernstein *et al.* [37,38] (see Table I). In the hydrodynamical limit of the collective model one expects $|M_n/M_p| = N/Z$. Deviations from this equality have been established in the past for semimagic nuclei (see, e.g., Ref. [37]).

The $B(E2)$ values determined in this work are plotted versus neutron number in Fig. 4 along with $B(E2)$ and $E(2_1^+)$ values for even-even Ni, Fe, and Cr isotopes. At $N = 28$, all isotopes display the large $E(2_1^+)$ energy and the small transition probability characteristics of a shell closure in even-even nuclei. However, only Ni, with a full $\pi 1f_{7/2}$ orbital, shows these indicators at $N = 40$. The decreasing energy values and increasing transition probabilities in the Fe and Cr chains are taken as direct experimental evidence for the onset of collectivity in the region below ^{68}Ni.

Shell-model calculations were performed using the LNPS interaction in a model-space consisting of the full fp shell for protons and the $1p_{3/2}$, $1p_{1/2}$, $0f_{5/2}$, $0g_{9/2}$, and $1d_{5/2}$ orbitals for neutrons [18]. For comparison, two additional sets of calculations were carried out using the well-established GXPF1A effective interaction [39,40] and LNPS restricted to the fp shell for both protons and neutrons. The results with the GXPF1A and restricted LNPS, hereafter denoted LNPS-fp, calculations were found to be nearly identical. To provide a consistent comparison between the fp and $fpg_{9/2}d_{5/2}$ valence spaces, we will refer to the LNPS-fp and LNPS interactions in the following.

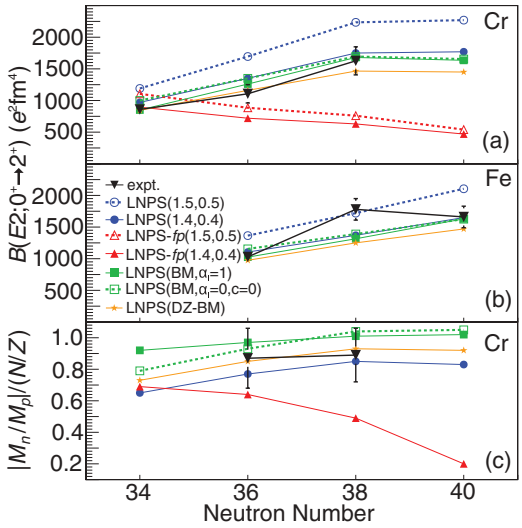

FIG. 5. (Color online) Comparison of measured $B(E2)$ transition strengths for Cr (a) and Fe isotopes (b), and ratios of $|M_n/M_p|$ relative to N/Z (c) with shell-model calculations. Shell-model calculations were performed using the LNPS [18] effective interaction in both the full model space, which included the $0g_{9/2}$ and $1d_{5/2}$ orbitals for neutrons (labeled LNPS), and a model space limited to the pf shell only (labeled LNPS-fp). The different choices of effective charges are indicated (see text for details).

The calculations are confronted with the experimental $B(E2;\ 0_1^+ \rightarrow 2_1^+)$ values in Fig. 5. The $B(E2)$ probabilities for ^{58,60,62}Cr in Fig. 5(a) are from this work and those quoted for ^{62,64,66}Fe [Fig. 5(b)] were taken from Ref. [19]. The trend of the theoretical $B(E2)$ values calculated using the LNPS amplitudes with the standard effective charges, $e_p = 1.5$, $e_n = 0.5$, correspond to the dashed line with open circles in Fig. 5(a). They agree with the trend exhibited by the Cr data, but the magnitude is overpredicted by 40–50%. For the iron data, the LNPS calculations with standard effective charges [dashed line with open circles in Fig. 5(b)] agree at $N = 38$, but again overpredict the $B(E2)$ values at $N = 36$ and $N = 40$. Using slightly reduced effective charges of $e_p = 1.4$ and $e_n = 0.4$ improves the overall agreement for both isotopic chains, although the calculations fail to describe the enhancement at $N = 38$ in the evolution of the $B(E2)$ values in the Fe chain. With these modified effective charges, the $B(E2)$ value of the key nucleus ^{64}Cr is predicted to be $B(E2;\ 0_1^+ \rightarrow 2_1^+) = 1770\ e^2\text{fm}^4$. As expected, a clear difference can be seen between the LNPS-fp and LNPS results. With increasing neutron number, excitations across the $N = 40$ gap become increasingly important. These excitations account for the onset of collectivity observed above $N = 36$ in the Cr isotopes, with large, nearly identical $B(E2)$ values predicted for ^{62}Cr and ^{64}Cr. In contrast, the LNPS-fp calculations follow the opposite trend, with $B(E2)$ values declining with increasing neutron number, reflecting the absence of the crucial $\nu 0g_{9/2}$ and $\nu 1d_{5/2}$ orbitals from the model space. The $|M_n/M_p|/(N/Z)$ values for ^{60,62}Cr are also compared with the calculations in Fig. 5(c). The measured $|M_n/M_p|$ values for both are around 0.9 (N/Z), indicating that the low-lying excitations follow the simple picture of protons and neutrons having the same deformation lengths with only a slight proton dominance relative to the simple hydrodynamical limit of N/Z. The LNPS calculations in the $fpgd$ space are consistent with these extracted ratios. In contrast, the LNPS-fp calculations predict a decreasing ratio towards $N = 40$, reflecting the occurrence of an $N = 40$ shell gap and highlighting again the inadequacy of the neutron model space in this Hamiltonian. All these observations are consistent with previous work that has demonstrated that the fp model space alone is inadequate to fully describe the low-lying structure in Cr isotopes heavier than ^{58}Cr because of the ever-increasing role of the $0g_{9/2}$ and $1d_{5/2}$ neutron orbitals [11,16,20,25,41]. In the LNPS effective interaction, the probability of neutron excitations to the $\nu 0g_{9/2}$ and $\nu 1d_{5/2}$ orbitals increases, going from $2p$-$2h$ excitations in ^{60}Cr to configurations dominated by $4p$-$4h$ excitations in ^{64}Cr, with sizable contributions of $6p$-$6h$.

Effective charges enter sensitively in the calculation of the theoretical transition strengths because $B(E2) = (e_p A_p + e_n A_n)^2/(2J_i + 1)$, where A_p and A_n are the proton and neutron shell-model amplitudes. The choices for e_p and e_n assumed for the discussion above are isoscalar and taken as constant across the isotopic chain. Effective charges compensate for missing excitations outside of the restricted shell-model space and it is not clear that the assumption of constant effective charges is valid throughout the entire model space. Bohr and Mottelson proposed N- and Z-dependent (isovector) effective $E2$ polarization charges that approximate the coupling to quadrupole modes outside of the model spaces of the effective interactions [44,45]. In the following, we use the Bohr-Mottelson (BM) formulation of the effective charges for the $B(E2) \sim M_p^2$ values as well as for the ratio of the proton and neutron transition matrix elements: $M_p = A_p(1 + \delta e_p) + A_n \delta e_n$ and $M_n = A_n(1 + \delta e'_n) + A_p \delta e'_p$, $\delta e_{p/n}$ and $\delta e'_{p/n}$ are the polarization charges following Bohr and Mottelson ($a = 1$, $b = -0.32$, $c = 0.32$, and $d = -0.65$) :

$$\delta e_{p/n} = a\frac{Z}{A} \pm c + \alpha_I \left[b\frac{N-Z}{A} \pm d\frac{Z}{A}\frac{N-Z}{A} \right], \qquad (1)$$

$$\delta e'_{p/n} = a\frac{N}{A} \pm c - \alpha_I \left[b\frac{N-Z}{A} \pm d\frac{N}{A}\frac{N-Z}{A} \right]. \qquad (2)$$

These expressions use an additional parameter, α_I, that scales the $(N - Z)$-dependent part so that $\alpha_I = 1$ gives the full BM values and $\alpha_I = 0, c = 0$ reduces it to the isoscalar part. Figure 5 shows the $B(E2)$ values and $|M_n/M_p|$ ratios calculated from the shell model using the BM effective charges for $\alpha_I = 1$ and $\alpha_I = 0, c = 0$. The calculations with the isovector $\text{BM}_{\alpha_I=1}$ polarization charges reproduce the Cr $B(E2)$ values within the experimental uncertainties with only small differences at $N = 34$ and 36 with respect to the isoscalar, $\alpha_I = 0, c = 0$, case. For the Fe isotopes, the differences between $\alpha_I = 0, c = 0$ and $\alpha_I = 1$ are even smaller and the results closely follow the calculations with constant effective charges $(e_p, e_n) = (1.4, 0.4)$. Significant differences become apparent for the $|M_n/M_p|$ ratios where the isoscalar and isovector BM polarization charges lead to differences of 15% for ^{58}Cr, where proton scattering data are unfortunately not available to deduce this quantity from experiment. While

the differences between $(e_p, e_n) = (1.4, 0.4)$, $\mathrm{BM}_{\alpha_I=1}$, and $\mathrm{BM}_{\alpha_I=0}$ are very small for the $B(E2)$ values, $|M_n/M_p|$ reveals significant potential to discriminate between the three different choices, with ^{58}Cr being most sensitive to the isovector part of the BM formulation and $(e_p, e_n) = (1.4, 0.4)$ values resulting consistently in significantly lower ratios across the isotopic chain.

As a next step we try to constrain the effective charges more microscopically and start with the $\delta e_{p/n}$ values proposed from dedicated shell-model studies [46,47] and evolve them as a function of $(N - Z)$ using the BM prescription. Dufour and Zuker (DZ) [46] obtain $(e_p, e_n) = (1.31, 0.46)$ in agreement with (1.36(5), 0.45(5)) deduced for the USD Hamiltonians [47]. Assuming that these values are good starting points at $N \sim Z$, we replace $aZ/A \pm c$ and $aN/A \pm c$ by constants so that $\delta e_p = \delta e'_n = 0.31$ and $\delta e_n = \delta e'_p = 0.46$ at $N = Z$. With this strategy and $\alpha_I = 0.8$ in Eqs. (1) and (2) and b and d from BM, the Cr and Fe $B(E2)$ values as well as the available $|M_n/M_p|$ ratios are described well. They are labeled LNPS (DZ-BM) in Fig. 5. The same calculation performed using the USD effective charges as $N = Z$ starting points instead of DZ gives results that agree within 5% or less with DZ (not shown). Again, although the $B(E2)$ values differ very little within the different scenarios discussed here for the effective charges, the $|M_n/M_p|$ ratios emerge as a quantity that can discriminate between the various approaches. In any event, the LNPS shell-model calculations of the $B(E2)$ values are very robust and rather consistently predict $B(E2; 0_1^+ \to 2_1^+) \sim 1600\ e^2\mathrm{fm}^4$ for the $N = 40$ key nucleus ^{64}Cr within 10%.

In summary, intermediate-energy Coulomb excitation of ^{58,60,62}Cr was performed and $B(E2; 0_1^+ \to 2_1^+)$ values were deduced from the measured cross sections. For ^{62}Cr, the $B(E2)$ excitation probability was also determined independently from a lifetime measurement that used a γ-ray line-shape analysis. Large-scale shell-model calculations with the LNPS effective interaction in a model space that includes the $0g_{9/2}$ and $1d_{5/2}$ orbitals for neutrons describe the trend of the data, but overestimate the magnitude of the quadrupole transition strengths when using the standard effective charges. Different choices of modified effective charges have been used to describe the onset of collectivity in the chromium isotopes approaching $N = 40$, with a robust prediction emerging for the $B(E2; 0_1^+ \to 2_1^+)$ value for the important nucleus ^{64}Cr. Nonstandard sets of effective charges were shown to provide an improved description of the known $B(E2)$ values in the Fe nuclei. The ratio of the neutron and proton transition matrix elements $|M_n/M_p|$, that can be deduced from combined proton scattering and Coulomb excitation data, reveals the potential to discriminate between different sets of effective charges in this model space.

This work was funded by the National Science Foundation under Contract No. PHY-0606007; by the US Department of Energy, Office of Nuclear Physics, under Contracts No. DE-AC02-06CH11357 and No. DE-FG02-08ER41556, and by the United Kingdom Science and Technology Facilities Council (STFC). A.P. is supported by the MICINN (Spain) (Grant No. FPA2011-29854) and by the Comunidad de Madrid (Spain) (Grant No. HEPHACOS S2009-ESP-1473).

[1] A. Gade and T. Glasmacher, Prog. Part. Nucl. Phys. **60**, 161 (2008).
[2] O. Sorlin and M.-G. Porquet, Prog. Part. Nucl. Phys. **61**, 602 (2008).
[3] T. Otsuka *et al.*, Phys. Rev. Lett. **87**, 082502 (2001).
[4] T. Otsuka, T. Suzuki, R. Fujimoto, H. Grawe, and Y. Akaishi, Phys. Rev. Lett. **95**, 232502 (2005).
[5] T. Otsuka *et al.*, Phys. Rev. Lett. **104**, 012501 (2010).
[6] C. J. Lister *et al.*, Phys. Rev. Lett. **59**, 1270 (1987).
[7] O. Sorlin *et al.*, Phys. Rev. Lett. **88**, 092501 (2002).
[8] D. Pauwels *et al.*, Phys. Rev. C **78**, 041307(R) (2008).
[9] A. Dijon *et al.*, Phys. Rev. C **85**, 031301(R) (2012).
[10] M. Hannawald *et al.*, Phys. Rev. Lett. **82**, 1391 (1999).
[11] A. Gade *et al.*, Phys. Rev. C **81**, 051304(R) (2010).
[12] M. Bernas *et al.*, Phys. Lett. B **113**, 279 (1982).
[13] C. Guénaut *et al.*, Phys. Rev. C **75**, 044303 (2007).
[14] S. Rahaman *et al.*, Eur. Phys. J. A **34**, 5 (2007).
[15] S. Zhu *et al.*, Phys. Rev. C **85**, 034336 (2012).
[16] E. Caurier *et al.*, Eur. Phys. J. A **15**, 145 (2002).
[17] L. Gaudefroy *et al.*, Phys. Rev. C **80**, 064313 (2009).
[18] S. M. Lenzi, F. Nowacki, A. Poves, and K. Sieja, Phys. Rev. C **82**, 054301 (2010).
[19] W. Rother *et al.*, Phys. Rev. Lett. **106**, 022502 (2011).
[20] J. Ljungvall *et al.*, Phys. Rev. C **81**, 061301(R) (2010).
[21] J. I. Prisciandaro *et al.*, Phys. Lett. B **510**, 17 (2001).
[22] A. Bürger *et al.*, Phys. Lett. B **622**, 29 (2005).
[23] N. Aoi *et al.*, Phys. Rev. Lett. **102**, 012502 (2009).
[24] A. N. Deacon *et al.*, Phys. Lett. B **622**, 151 (2005).
[25] S. Zhu *et al.*, Phys. Rev. C **74**, 064315 (2006).
[26] A. N. Deacon *et al.*, Phys. Rev. C **83**, 064305 (2011).
[27] D. J. Morrissey *et al.*, Nucl. Instrum. Methods Phys. Res., Sect. B **204**, 90 (2003).
[28] D. Bazin *et al.*, Nucl. Instrum. Methods Phys. Res., Sect. B **204**, 629 (2003).
[29] J. Yurkon *et al.*, Nucl. Instrum. Methods Phys. Res., Sect. A **422**, 291 (1999).
[30] W. F. Mueller *et al.*, Nucl. Instrum. Methods Phys. Res., Sect. A **466**, 492 (2001).
[31] S. Agostinelli *et al.*, Nucl. Instrum. Methods Phys. Res., Sect. A **506**, 250 (2003).
[32] T. Glasmacher, Annu. Rev. Nucl. Part. Sci. **48**, 1 (1998).
[33] A. Winther and K. Alder, Nucl. Phys. A **319**, 518 (1979).
[34] C. Zhou, Nucl. Data Sheets **76**, 399 (1995).
[35] A. L. Nichols, B. Singh, and J. K. Tuli, Nucl. Data Sheets **113**, 973 (2012).
[36] L. A. Riley *et al.*, Phys. Rev. C **72**, 024311 (2005).
[37] A. M. Bernstein, V. R. Brown, and V. A. Madsen, Phys. Lett. B **103**, 255 (1981).
[38] A. M. Bernstein, V. R. Brown, and V. A. Madsen, Comments Nucl. Part. Phys. **11**, 203 (1983).

[39] M. Honma, T. Otsuka, B. A. Brown, and T. Mizusaki, Phys. Rev. C **65**, 061301(R) (2002).
[40] M. Honma *et al.*, Eur. Phys. J. A **25** s1, 499 (2005).
[41] S. J. Freeman *et al.*, Phys. Rev. C **69**, 064301 (2004).
[42] B. Pritychenko *et al.*, Brookhaven National Laboratory Report BNL-94720-2011-JA, 2011.
[43] M. Seidlitz *et al.*, Phys. Rev. C **84**, 034318 (2011).
[44] A. Bohr and B. R. Mottelson, *Nuclear Structure*, Vol. 2 (Benjamin, New York, 1975).
[45] H. Sagawa, T. Suzuki, and K. Hagino, Nucl. Phys. A **722**, c183 (2003).
[46] M. Dufour and A. P. Zuker, Phys. Rev. C **54**, 1641 (1996).
[47] W. A. Richter, S. Mkhize, and B. A. Brown, Phys. Rev. C **78**, 064302 (2008).